Exploring structure dependencies of gas-surface interactions with curved single crystals

Auras, S.V.

7

OUTLOOK

In chapter 2, we have shown recent advances in the applications of curved crystals exploring magnetic, electronic and chemical properties of vicinal surfaces. Our group has made significant advances in gas-surface reaction dynamics by revealing site-specific reactivity and surface structure effects - initially by using flat single crystals with stepped surfaces, and progressively by incorporating curved crystals with tunable surface structures.[1–4]

This thesis exclusively covers work on curved single crystal surfaces. We have illustrated their benefits when studying gas-surface reactions. Specifically, cylindrical slices of Ag and Pt single crystals were employed to study the effect of surface structure on elementary reaction steps, e.g. dissociative adsorption or molecular desorption. This chapter provides an outlook on on-going experiments employing curved single crystals that were initiated during the course of this PhD project. These include research on CO_2 adsorption on stepped and kinked Pt surfaces, with the goal of studying structure-dependent CO_2 dissociation. We are also investigating a novel curved crystal surface comprised of an ordered bimetallic alloy, i.e. *c*-NiAl(110)[001]-31°.

7.1. EXPLORING REACTIVE SITES TOWARDS CO_2 DISSOCIATION

RISING CO_2 LEVELS in the atmosphere and depleting fossil fuel reserves are two faces of the same global challenge we are currently confronted with. The first model linking atmospheric CO_2 levels to global climate was developed by Arrhenius in the 19th century.[5, 6] In this context, capturing and converting CO_2 to higher-value chemicals presents an attractive alternative. However, CO_2 is the final product of all oxidation processes involving carbon species, being inherently thermodynamically stable. On a molecular level, two C=O double bonds require substantial energy to break, before any other molecular species can be formed. A catalyst, by definition, cannot change the thermodynamics of a chemical reaction; CO_2 conversion remains an endothermic reaction, even at a catalytic surface. However, the activation energy of the process can be lowered by a catalyst, improving the energetic cost of possible applications. A commonly proposed pathway is the reduction of CO_2 to CO. CO could then subsequently be converted into larger hydrocarbon chains by the Fischer-Tropsch reaction.

For CO formation from CO_2, the probability of bond breaking is expected to increase if the asymmetric C=O stretch vibration is excited when the molecule hits the catalyst's surface. Our group is currently initiating experiments to measure state-resolved CO_2 dissociation using the supersonic molecular beam. The asymmetric stretch vibration of CO_2 is stimulated using a laser at the vibrational eigenfrequency (2350 cm^{-1}), with the goal of measuring the vibrational efficacy:

$$CO_2^{\nu_3} + 2* \rightleftharpoons CO_{ads} + O_{ads} \tag{7.1}$$

It is therefore prudent to first study CO_2 sticking without vibrational excitation. As a first step, we have explored structure dependencies of molecular CO_2 adsorption on Pt surfaces vicinal to (111). Pt is a commonly used catalyst for the CO oxidation reaction, which can be considered the reverse of equation 7.1.

We combine the two curved Pt crystals also used in chapter 4, *c*-Pt(111)[1$\bar{1}$0]-31° and *c*-Pt(111)[11$\bar{2}$]-31°, to study CO_2 sticking on stepped and kinked Pt surfaces. They each expose the (111) plane at the apex and curve 15.5° to each side, thereby introducing close-packed or highly kinked steps respectively. We impinge a molecular beam of pure CO_2 onto the surfaces. From time-of-flight measurements, a beam energy of 77.5 meV is determined. The beam impinges on the crystal surface with a rectangular imprint to improve spatial resolution along the curvature, as discussed in chapter 4. For the experiment, both crystals are cooled with super-cooled liquid nitrogen, resulting in a measured surface temperature of 81 K for the crystal with A- and B-type steps and 87 K for the crystal with {210} steps. At these temperatures, CO_2 is expected to physisorb on Pt.[7, 8] We attribute the temperature difference to

different thermal conductance of the sample holder after exchanging the crystals, in addition to small changes in the thermocouple connections. Initial sticking probabilities (S_0) are obtained by the King-and-Wells method.[9] Measurements are carried out sequentially at different positions of the curved crystal. As surface chirality is not expected to influence reactivity for this system, results obtained on the two side of the *c*-Pt(111)[11$\bar{2}$]-31° crystal are averaged.

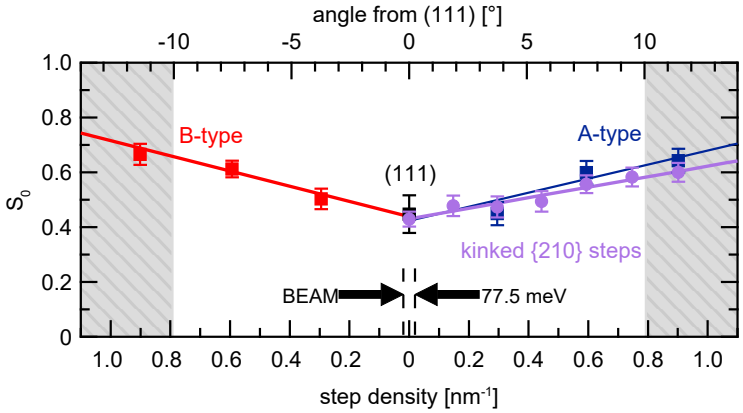

Figure 7.1: Initial sticking probabilities of a supersonic molecular beam of CO_2 (77.5 meV) obtained on the surfaces of two curved Pt crystals. For the *c*-Pt(111)[1$\bar{1}$0]-31° crystal (blue, red, black), sticking probabilities are measured at T_{surf} = 81 K. Sticking probabilities on the *c*-Pt(111)[11$\bar{2}$]-31° crystal (purple) are measured at T_{surf} = 87 K. Grey areas of the plot indicate where the surface width becomes more narrow than the beam width. Only data in the white area of the plot are included in the linear fits for each step-type (solid lines). Black arrows and dashed lines indicate the size of the beam along the curvature of the crystal.

Figure 7.1 plots initial sticking probabilities (S_0) of CO_2 on the Pt surfaces as a function of step density. At the apex of the two different crystals, $S_0^{(111)}$ is measured as 0.447 and 0.429, confirming that results from the two crystals are comparable despite slightly different surface temperatures. This sticking probability is in good agreement with $S_0^{(111)}$ values determined by Kulginov *et al.* at comparable kinetic energies.[10] For all three step types, S_0 increases with step density. This mirrors results on other metallic surfaces where low-Miller index planes are found to be particularly inert towards physisorption of CO_2, while lower coordinated sites or surfaces with co-adsorbed alkali metals are more reactive.[8, 11, 12]

The physisorption well for CO_2 on Pt(111) is about 0.2 eV.[10] Sticking can be seen as a two-step process, where a molecule approaching the surface may first get trapped and must subsequently equilibrate its energy with the surface. Trapping in this well can occur by transferring incident translational energy into rotational or vibrational motion, or lattice vibrations. Molecules getting trapped must quickly dissipate their (normal) translational energy, or they desorb again without sticking. However, for CO_2 on Pt(111), energy transfer to lattice vibrations is limited to ~0.55 eV, and vibra-

tional excitation was negligibly small for E_i <1 eV.[10] In an earlier study, sticking was found to be reasonably high ($S_0 = 0.6$) at low incident kinetic energies of ~60 meV.[10] With increasing kinetic energy, initial sticking probabilities decrease quickly, due to limited energy dissipation in the relatively shallow well. However, a high-energy tail remains and S_0 never reduces to zero, even at energies >1 eV. This phenomenon was attributed to improved translational to rotational coupling at high energy.

We see two possible mechanisms for improved sticking of CO_2 at vicinal surfaces for the low kinetic energy that was probed here (77.5 meV). Firstly, edges may improve the conversion from normal to lateral motion during the initial trapping. However, this may still result in desorption, as the translational energy is preserved in the collision. Secondly, steps may improve translational to rotational coupling already at lower kinetic energies than for the flat surface, and thus improve the sticking probability. Coupling to vibrational modes is unlikely here, as even the lowest molecular vibrational mode, the bend mode, has a frequency of 83 meV on the Pt(111) surface.[13] Only a small portion of molecules, at the higher end of the kinetic energy distribution in our beam, could thus be vibrationally excited.

We fit the data of S_0 in figure 7.1 for each step type with a linear function:

$$S_0(SD) = S_0^{(111)} + \Sigma_0 \cdot SD \tag{7.2}$$

Data in the grey area of the plot, where the rectangular beam is wider than the available crystal surface, is excluded from the fits. Fits yield S_0 values of 0.423, 0.439, and 0.430 for the ideal, defect-free (111), in good agreement with the results on the as-prepared (111) surface of the two crystals. The slopes of the fits (Σ_0) are 0.256 nm, 0.277 nm, and 0.192 nm for A-type, B-type and {210} steps respectively. Table 7.1 summarises these results.

In chapter 4, we converted Σ_0 to reaction cross-sections (σ_0^{step}) for dissociation of D_2 at steps, corresponding to the reactive area in the potential energy surface (A) near the step. This interpretation works well at low kinetic energy, where sticking at terraces is low and the sticking probability when impinging on the area A is approximately unity. At higher kinetic energies, the indirect mechanism to dissociation at steps is reduced. The experimentally determined reaction cross-section (σ_0^{step}) may then be smaller than A, due to the reduced efficacy of dissociation.[14] The experimentally determined reaction cross-section (σ_0^{step}) is then the product of the reactive area (A) of the potential energy surface and the probability of dissociation when a molecule impinges on this area (S_0^A):

$$\sigma_0^{step} = S_0^A \cdot A \tag{7.3}$$

A similar model may be applicable to link the cross-sections σ_0 for CO_2 sticking at step edges, as determined from the slopes Σ_0, to the potential energy surface for CO_2 adsorption on vicinal Pt surfaces.

crystal	$S_0^{(111)}$ experimentally	step-type	$S_0^{(111)}$ from fit	Σ_0 from fit
c-Pt(111)[1$\bar{1}$0]-31°	0.447	A / {001}	0.423	0.256 nm
		B / {110}	0.439	0.277 nm
c-Pt(111)[11$\bar{2}$]-31°	0.429	{210}	0.430	0.192 nm

Table 7.1: Results for CO_2 sticking from a 77.5 meV beam on Pt surfaces on two curved crystals.

Differences in sticking efficiency of the three step-types cannot be conclusively discussed here due to the limited number of probed surfaces. Future studies varying kinetic energies, and probing more points across the curved surface is expected to yield more detailed insights into the mechanism of CO_2 sticking on Pt and the role of specific surface sites.

In addition to CO_2 adsorption we have also studied the molecular desorption of CO_2 from vicinal Pt surfaces. Figure 7.2 shows preliminary results of temperature-programmed desorption of CO_2 from the *c*-Pt(111)[11$\bar{2}$]-31° crystal with {210} steps. CO_2 was dosed with the molecular beam for 180 s at different positions along the curved surface at 91 K. During a subsequent temperature ramp of ~1 K/s, CO_2 desorption was detected with a quadrupole mass spectrometer. The rate of desorption from a surface is given as:[2]

$$r(\theta) = -\frac{\mathrm{d}\theta}{\mathrm{d}t} = \nu_{des} \cdot \theta^n \cdot e^{-\frac{E_{des}}{RT}} \tag{7.4}$$

Here, r is the reaction rate, θ is the surface coverage, t is time, ν_{des} is the attempt frequency, n is the order of desorption, E_{des} is the desorption energy, R is the universal gas constant, and T is temperature.

For multilayer desorption of CO_2 from graphene-covered Pt(111), 0^{th} order kinetics were recently determined.[15] While we cannot confirm the desorption order definitively without varying coverage, the desorption traces in figure 7.2b) indicate similar kinetics here. In the assumption of 0^{th} order kinetics, plotting the natural logarithm of the desorption signal against the inverse of the desorption temperature in figure 7.2 allows us to determine the desorption energies, according to equation 7.4. Values for E_{des} obtained at different parts of the surface range from 24.7 kJ/mol to 38.8 kJ/mol.

Due to the large doses in the experiment, the desorption signal must stem largely from CO_2 molecules desorbing from layers of CO_2 ice. The desorption energies in figure 7.2c) reflect this: they resemble the enthalpy of sublimation (ΔH_s) for CO_2 under standard conditions, 28.8 kJ/mol.[16] Accordingly, no clear variation with step density can be observed.

Supplementary TPD experiments for smaller doses are expected to further elucidate

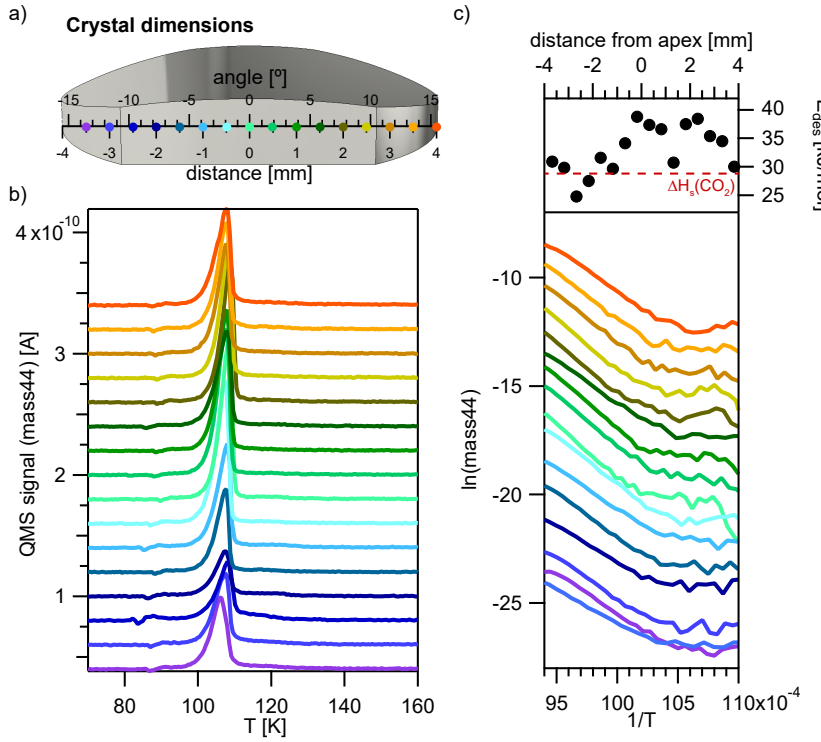

Figure 7.2: a) Schematic drawing of the *c*-Pt(111)[11$\bar{2}$]-31° crystal and its dimension. Circles mark the position on the surface where TPDs were recorded. b) QMS signal of mass 44 during temperature-programmed desorption of CO_2 from different parts of the crystal. c) Arrhenius plot of desorption data in b) and desorption energies obtained from fits to the linear parts of the traces. ΔH_s indicates the standard enthalpy of sublimation of solid CO_2.

7

adsorption energies at steps and terraces. However, detecting low coverages of CO_2 desorbing from the small surface area covered by the rectangular molecular beam is expected to be challenging. Instead, the apparatus described in chapter 6 is better suited for spatially-resolved TPD experiments involving small doses of CO_2.

7.2. DETERMINING ADSORPTION SITES AND STRUCTURES BY LOW-TEMPERATURE STM

Combining low-temperature STM with curved crystals opens new possibilities to resolve adsorption sites and adsorption structures of molecules and to observe the effects of increasingly narrow terraces on adsorption.

We have investigated adsorption of CO_2 on stepped Pt surfaces in a low-temperature STM study of the *c*-Pt(111)[1$\bar{1}$0]-31° crystal at Loyola University in Chicago, USA. The experimental set-up has previously been described in detail by the Loyola group.[17, 18] In short, the apparatus consists of a preparation and an STM chamber. Surface preparation of the curved Pt crystal is performed according to the procedure described in chapter 4 and the progress of surface preparation is monitored by LEED. In the preparation chamber, the sample can only be cooled to 110 K using a liquid nitrogen cryostat. As we have shown in figure 7.2, this temperature is above onset of desorption for CO_2. Therefore, the freshly prepared sample is transferred first to the STM, which is cooled by a close-cycle He cryostat. First, the clean surface is imaged at 30 K at different points across the surface. In figure 7.3, we find regular step arrays. Only close to the apex steps deviate from the expected step direction due to meandering. After cleaning the surface again, transferring, and cooling the sample to 30 K in the STM cryostat, CO_2 is background dosed onto the crystal. The surface is then imaged again after exposures of 1 L and 3 L.

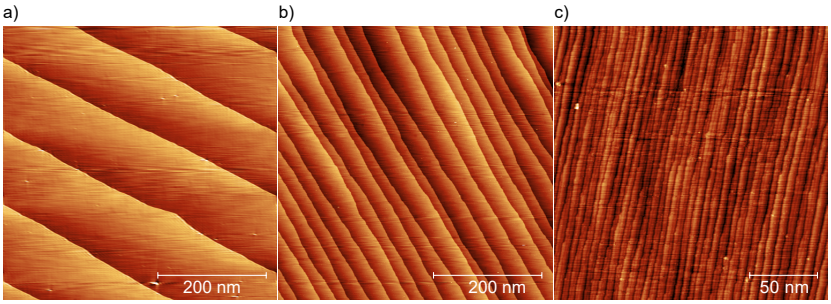

Figure 7.3: STM images after surface preparation of surfaces featuring wide and narrow step arrays, before dosing of CO_2.

CO_2 molecules cannot be atomically resolved but the entire molecule appears as a round bright protrusion instead, as shown in figure 7.4. After the 1 L dose, STM images show molecules evenly dispersed on the Pt(111) terraces. On wide terraces, no clustering or formation of adsorbate structures is observed. CO_2 diffusion is reported to be slow in the few instances where it has been studied.[8] Here, we observe no ordering or clustering of molecules on the terraces appears on wider terraces even days after dosing. The (3 × 3) structure previously reported for CO_2 on Pt(111) could not be observed.[7] On stepped images, however, CO_2 molecules are observed dec-

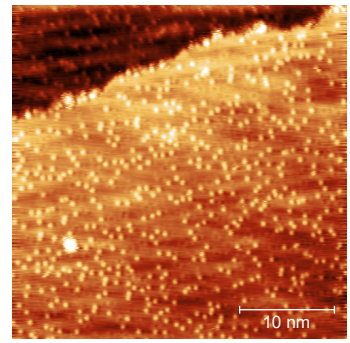

Figure 7.4: 35 nm×35 nm STM image near the apex of the curved crystal after dosing 1 L of CO_s.

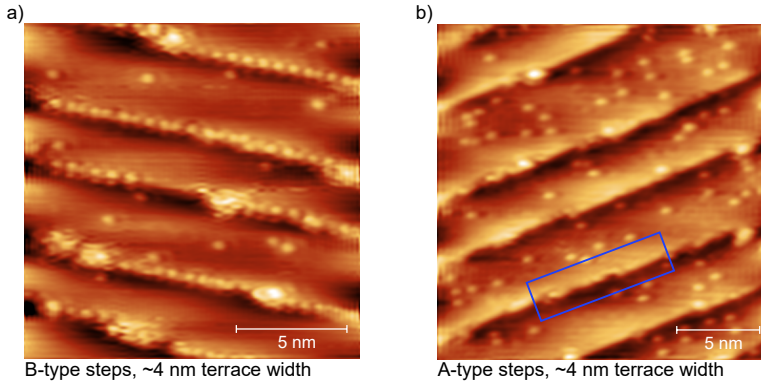

Figure 7.5: STM images of surfaces on the *c*-Pt(111)[1$\bar{1}$0]-31° crystal, after dosing 1 L CO_2 at 30 K. a) 15 nm×15 nm image with B-type steps, on ~4 nm wide (111) terraces. Individual molecules are observed on the terraces, and resolved decorating the step edges. b) 15 nm×15 nm image with A-type steps, on ~4 nm wide (111) terraces. Molecules are resolved on the terraces but not along the steps. Instead, bright lines appear along the step edges. The blue rectangle highlights part of a step edge where adsorbates at the step edge are just barely resolved.

7

orating the step edges and in some instances forming larger clusters. They appear either molecularly resolved or as bright stripes along the step edge, as illustrated in figure 7.5. However, height profiles across the steps reveal that the bright step edges are also covered. Terraces on highly stepped surfaces appear depleted of molecules, indicating that diffusion on the Pt(111) terraces indeed occurs, but does not lead to ordered structures on the terraces.

In figures 7.6 and 7.7, we extract line profiles along step edges for two images where molecules are resolved at the steps. We obtain the distance between the molecules, which appear as rounded peaks in the line profiles, to determine their intermolecular spacing. From figure 7.6, after the 1 L dose, an average value of 6.46 Å is found. In figure 7.7, molecules are spaced on average 6.63 Å apart. The additional dosing of CO_2 thus does not change the coverage at steps. This spacing does not match well with Pt atomic spacings along the step edge (n×2.77 Å).

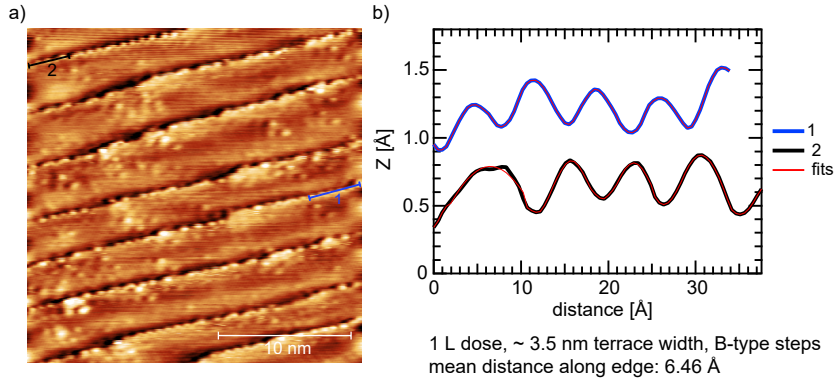

Figure 7.6: a) 25 nm×25 nm STM image of a surface with B-type steps on ~3.5 nm wide terraces, after a 1 L dose of CO_2 at 30 K. Blue and black lines indicate where line profiles were taken to determine spacing of molecules along the step edge. b) Line profiles (blue, black) extracted from the image. Multiple gaussian fits (red) are used to determine centers of peaks and consecutively distances between molecules.

While it would be interesting to determine structure dependent coverages and changes relating to different doses, we encounter the challenge that molecules at step edges are not always resolved. We therefore have to quantify coverage on the terraces and changes with step density, in order to deduce the relative coverages at steps. We have initiated a collaboration with the theory group in Leiden, to develop an algorithm to identify molecules on terraces and train it by machine learning. The goal is to quantify coverages for a high number of STM images and obtain statistically relevant results regarding effects of step density, step type, and CO_2 dose. Figure 7.8 shows current results of the training process. The aim is to train the algorithm so that it can detect molecules on terraces with the same accuracy as a human would by eye.

On some of the stepped surfaces we observe the bright features as 'dimers' (after the 1 L dose) or 'trimers' (after the 3 L dose), instead of monomers. In specific instances they appear to form larger ordered structures. Figure 7.9a) shows an STM image where "dimers" are covering all three terraces. In figure 7.9b) the contrast of the middle terrace is adjusted to make more details visible. The dimers appear approximately in parallel to each other and follow the same internal structure with one protrusion brighter than the other one. From line profiles we obtain average "C-C distances" of 6.57 Å within these clusters. Figures 7.9c) and d) show surfaces where "trimers" were observed. Again, they cover all terraces in the image. They form triangles that are aligned in the same direction relative to the step edges, and scale with the image size. Line profiles give an average of 4.28 Å. Figure 7.9e) shows the distributions of these distances, separated by the directions in the cluster, for trimers in d). Notably, one direction, approximately parallel to the steps, is larger than the other two in all clusters.

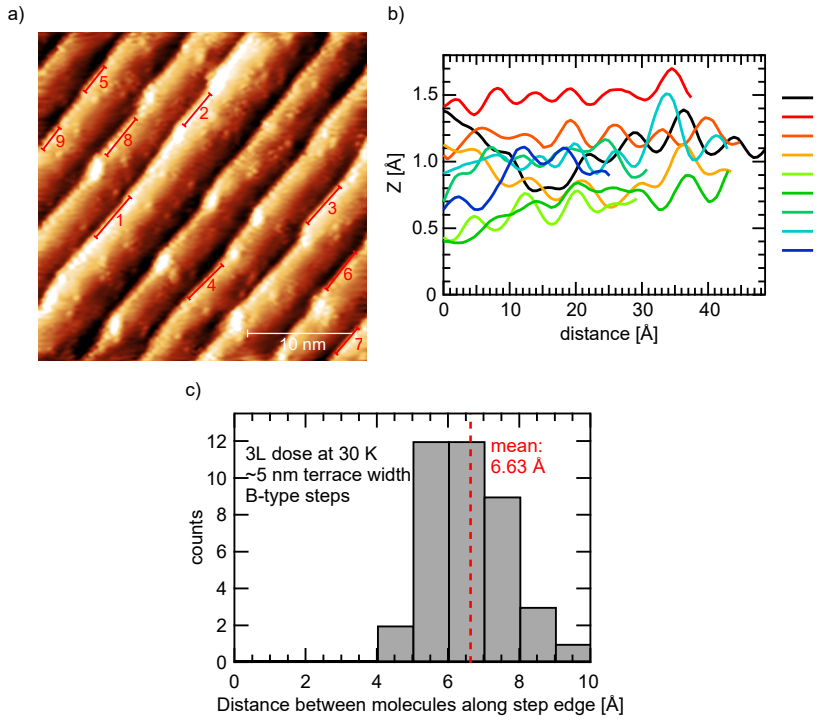

Figure 7.7: a) 25 nm×25 nm STM image of a surface with B-type steps on ~3.5 nm wide terraces, after a 3 L dose of CO_2 at 30 K. Red lines indicate where line profiles were taken to determine spacing of molecules along the step edge. b) Line profiles extracted from the image. c) Distribution of molecule spacings along step edges.

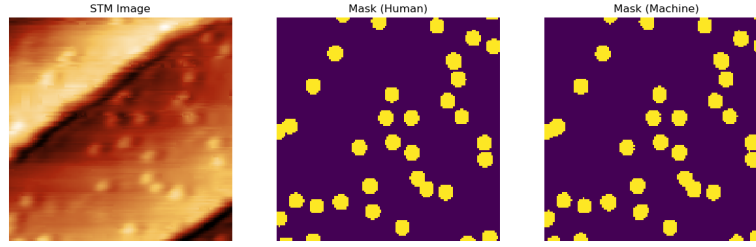

Figure 7.8: STM image used to train the machine learning algorithm to recognize and count molecules on terraces. Left: the original image. Middle: Mask created from molecules detected by human eye. Right: Mask found by algorithm. Figure by Paul Spiering.

Trimers of adsorbed CO_2 have previously been observed in STM studies on Ru(0001) and Ni(110).[19, 20] They also occur in gas-phase CO_2.[21] In the gas-phase, C-C distances of 3.60 Å and 4.03 Å are reported for dimers and trimers respectively. For the CO_2 trimers on Ru(0001) and Ni(110), effects of the underlying terrace on the orientation of clusters have been observed. On Ru(0001), CO_2 was adsorbed at (three-fold

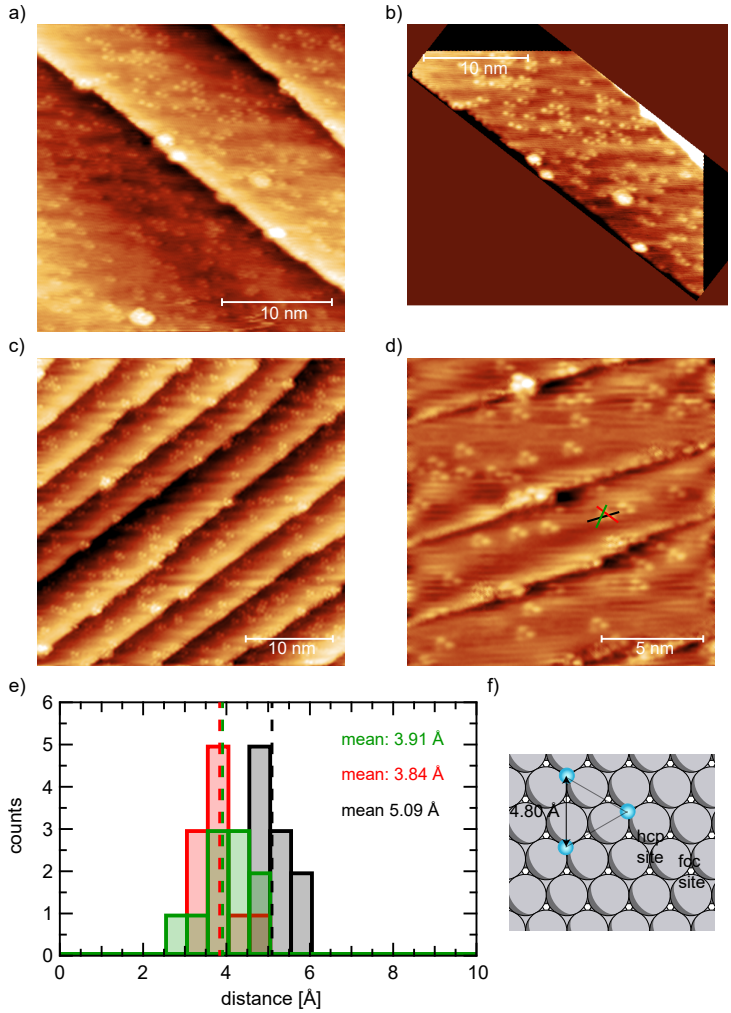

Figure 7.9: a) 30 nm×30 nm STM image where protrusions appear as "dimers" on terraces (B-type steps) after a 1 L dose of CO_2. b) Middle terrace of image a), contrast adjusted. c) 35 nm×35 nm STM image where "trimers" cover ~4.5 nm wide terraces (A-type steps) across a larger surface area, after a 3 L dose. d) 15 nm×15 nm STM image taken in the same position, showing well resolved trimer clusters. Red, green, and black lines indicate axes along which C-C distances were determined. e) Distributions of C-C distances in clusters in image d), separated by directionality. Colours of the bars correlate lines in d). f) Suggested sites of adsorption of CO_2 on Pt(111).

hollow) *hcp* sites.[19] The trimer orientation therefore switched on adjacent terraces due to the stacking order of the hcp lattice. Similarly, CO_2 was adsorbed at hollow sites of the Ni(110) surface.[20] The distance for protrusions within trimers we observe on the Pt(111) terraces, 4.28 Å, potentially indicates adsorption on next-nearest *hcp* sites, as illustrated in figure 7.9f).

We must note, however, that in the STM images where we observe dimeric or trimeric

protrusions on narrow terraces, these clusters appear very uniform in size and shape. Furthermore, only few monomers can be found in these images. The "dimers" and "trimers" could therefore also be artifacts of imaging with a double or triple tip. On the other hand, step edges appear crisp and absent of doubling effects, and CO_2 adsorbed at steps can still be observed as single protrusions. Future experiments are recommended to confirm the formation of dimer and trimer clusters on these stepped surfaces.

7.3. INTRODUCING CURVED CRYSTALS OF BIMETALLIC ALLOYS

So far, curved crystals cut from single-crystalline metals are by far the most commonly employed type. However, their use does not have to be limited to this material type. Recently, curved crystals of metal oxides, which are common materials for industrial heterogeneous catalysts, have been studied.[22, 23] In another instance, curved Ag crystals were used to grow a stepped bimetallic alloy.[24] Here, we examine the curved surface of a bulk bimetallic alloy, NiAl.

NiAl crystallizes in the CsCl crystal structure, i.e. a body-centered cubic lattice of two distinct types of atoms. The (110) plane, as displayed in figure 7.10a), consists of alternating rows of the two elements. For NiAl(110), the surface is not a perfect bulk termination. Instead, Ni atoms are slightly relaxed towards the bulk and Al atoms are elevated out of plane, causing a rippled structure with a 0.22 Å height displacement between rows of Ni and Al.[25] Surface oxidation of NiAl(110) results in the formation of Al_2O_3. Alumina is often used as an oxide support for catalytic nanoparticles in industrial catalysts. The surface science approach to heterogeneous catalysis frequently makes use of NiAl to grow well-ordered films of Al_2O_3. In this way, the behavior of the surface oxide can be studied, while maintaining a conducting metallic bulk, which is essential to many electron-based surface-science techniques. While on NiAl(110) different rotational domains of Al_2O_3 are formed, the introduction of step edges on vicinal surfaces can aid in aligning these domains.[26, 27]

Vicinal surfaces of bare NiAl also present an interesting fundamental problem regarding to their surface properties. First, we introduce the sample and its surface structure. The crystal we study can be considered a 31° slice of a cylinder curved around the [001] axis, exposing NiAl(110) at its apex, as figure 7.10b) illustrates. Following the nomenclature introduced in chapter 2, we refer to it as *c*-NiAl(110)[001]-31°. Steps introduced towards the side of the crystal therefore form {100} microfacets, consisting of rows of the same atom type at the upper and lower step edges, as shown in figure 7.10a). The problem referred to above is then as follows: As essentially a microfacet of only one element type is formed at the steps, it may be assumed that steps of either Ni or Al are preferred. NiAl(001) surfaces have been reported to terminate

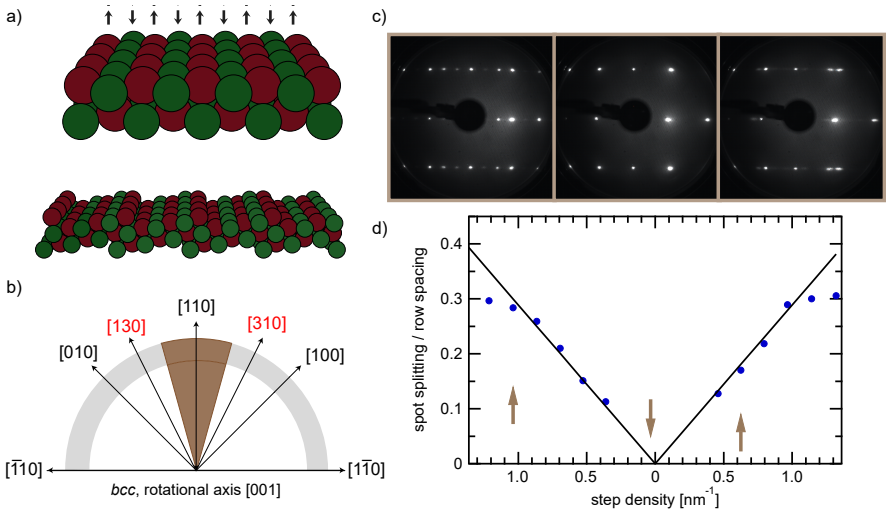

Figure 7.10: a) Schematic structure of NiAl(110). Instead of a perfect bulk termination, Al rows (red) are displaced slightly above the Ni atoms (green). Below, example of the stepped surfaces with {100} steps found on the *c*-NiAl(110)[001]-31° crystal. b) schematic drawing of the cylinder that the crystal slice is cut from. c) LEED images from different parts of the curved crystal, showing a (110) diffraction pattern (center), and spot splitting caused by regularly stepped surfaces (left, right) d) Spot splitting over row spacing ratios determined at different parts of the surface (blue circles), and expected ratios (black lines). Arrows indicate positions of LEED patterns in c).

preferentially on Ni planes.[28] If indeed one type of element is preferred at the step edges, on our crystal the Ni:Al ratio of surface atoms should gradually shift away from the 50:50 ratio at the (110) surface. Surface sensitive techniques, e.g. XPS and AES, are expected to detect this shift. A preferred registry of terrace widths may also be observable in terrace width distributions from STM images.

Surface preparation of this crystal has proven to be extremely sensitive to background pressures of O_2 and H_2O, as well as temperature. However, we can now prepare clean surfaces across the entire range of the curved crystal. Figure 7.10c) depicts LEED patterns from the (110) apex, as well as the sides. LEED spots are well-defined and distinct split spots appear at the stepped surfaces. In figure 7.10d) we confirm that spot splitting to row spacing ratios follow the expected trend. Expected spot splitting to row spacing ratios were determined according to table 2.1 in chapter 2.

An STM study of the *c*-NiAl(110)[001]-31° crystal was carried out at the Materials Physics Center in San Sebastián, Spain. The apparatus is a variable temperature setup similar to the one described in chapter 6. While meandering step edges are observed at the apex, steps start aligning at very small miscut angles, where they separate wide (110) terraces, as figure 7.11a) shows. As step density increases, we find regularly stepped surfaces. In figure 7.11b), step edges follow predominantly the direction that is expected as a result of the crystal's curvature. Kinks occur occasionally

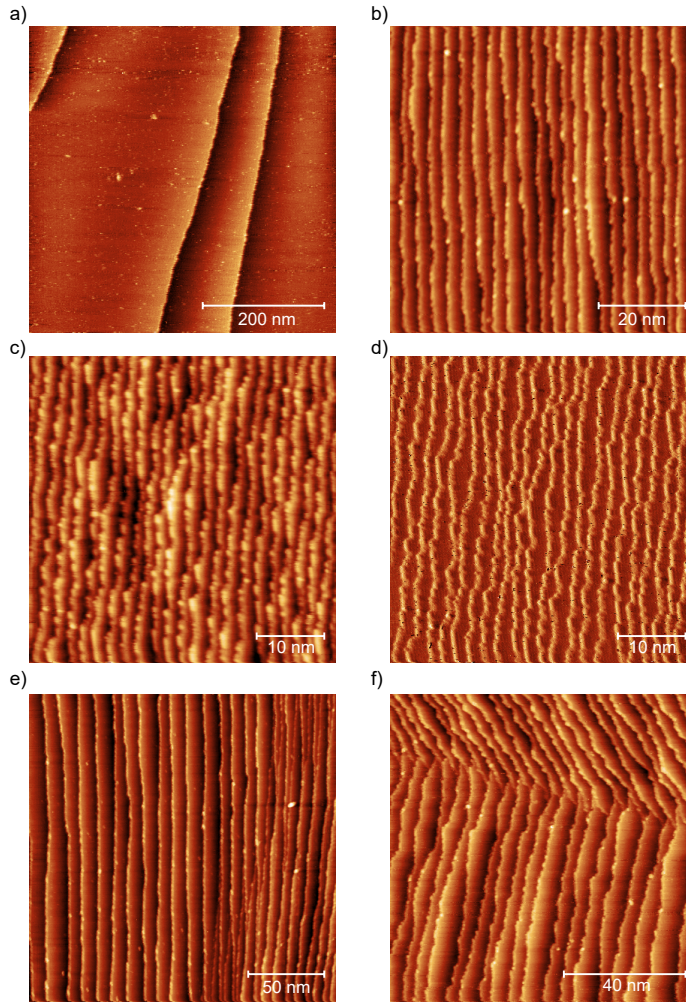

Figure 7.11: STM image take across the *c*-NiAl(110)[001]-31° crystal. a) Wide terraces are found close to the apex. b) Towards the sides of the crystal, narrow terraces form regularly stepped arrays. c) Step edges on the vicinal surfaces can be difficult to trace in the Z-channel of the image. d) In the I-channel of the same image, step outlines are more clearly detectable. e) On some surfaces step bunching occurs. f) Step edges deviating from the expected orientation and changing directions.

but the majority portion of each step runs parallel to the [001] vector.[1] We observe that step edges often appear brighter than terraces. The bright protrusions hinder determination of outlines of step edges at narrower terraces, as illustrated in figure 7.11c). For statistical analysis of terrace widths and kinks in steps, as done in chapter 3, it is thus more useful to use the I-channel of these images. In figure 7.11d) the outlines of step edges reveal that kinks here occasionally cause larger deviations from the ex-

[1] Surface vectors and step types on the NiAl(110) surface are consistent with those illustrated for *bcc*(110) surfaces in figure 2.3.

pected step direction, along the direction of close-packed steps. The group has currently started a through analysis of STM images with the goal of determining whether one element is preferred at the step edge by identifying preferred terrace widths.

While regularly stepped arrays are found predominantly, we occasionally find surfaces that diverge from the expected structures. In figure 7.11e), step bunching occurs on the right side of the image, but regularly stepped, wider terrace recur in the left part of the image. A more curious phenomenon is displayed in figure 7.11f). There, steps in the top part of the image have a different orientation than steps at the bottom part. Both directions deviate from the ideal step direction given by the curvature, i.e. vertically in the image. However, in both parts steps run in parallel to other steps and appear to form ordered arrays. Where they meet, a small overlap of steps in both directions is observed. The relative orientation of the two types of step array suggest the formation of close-packed {211} microfacets, rather than the more open {100} steps here. The cause of the structural transformation is not clear.

Further exploration of structural phenomena on vicinal NiAl surfaces may give insight into the role of terrace width and lateral confinement by steps on the resulting surface structure of this interesting phenomenon. Supplementary AES/XPS studies may elucidate whether minute surface contaminations induce structural changes. A thorough understanding of this surface is required before initiating experiments regarding chemical reactivity.

7.4. POSSIBLE FUTURE APPLICATIONS OF CURVED CRYSTALS

Beyond on-going research presented in this chapter, curved crystals have extensive potential in studying structural effects in surface chemistry. Their variable surface structure could be a useful tool, e.g. when studying reactions in which diffusion between reactive sites plays an important role, or reactions involving multiple reactants with different affinity to surface sites. Curved crystals exposing chiral surfaces, like the *c*-Pt(111)[11$\bar{2}$]-31° crystal we have extensively studied, may prove valuable on the path towards efficient chiral catalysis. Orientations in between close-packed and fully-kinked step directions, may be preferable for larger chiral reactants, e.g. amino acids.

Lastly, we would like to emphasize the value of combining multiple curved crystals, as demonstrated in chapters 4 and 6. This approach allows exploration of a large range of surfaces, when dome-shaped samples or full cylinders are not feasible. Combination of cylindrical slices make it possible to target particularly interesting ranges, and avoid multiples of the same surface structure.

REFERENCES

[1] A. den Dunnen. *Surface-structure dependencies in catalytic reactions.* PhD thesis, Leiden University, 2015.

[2] C. Badan. *Surface-Structure Dependence of Water-Related Adsorbates on Platinum.* PhD thesis, Leiden University, 2016.

[3] K. Cao. *Structure dependence of molecular reactions on surfaces.* PhD thesis, Leiden University, 2018.

[4] R. van Lent. *Steps in gas-surface reactions.* PhD thesis, Leiden University, 2019.

[5] S. Arrhenius. On the Influence of Carbonic Acid in the Air upon the Temperature of the Ground. *The Philosophical Magazine*, 41:237–276, 1896.

[6] S. Arrhenius. Über den Einfluss des atmosphärischen Kohlensäurengehalts auf die Temperatur der Erdoberfläche. *Bihang till Kungl. Svenska Vetenskapsakademiens handlinga*, 22:1–102, 1896.

[7] C.-L. Kao, A. Carlsson, and R. J. Madix. The adsorption dynamics of molecular carbon dioxide on Pt(111) and Pd(111). *Surface science*, 497(1-3):356–372, 2002.

[8] U. Burghaus. Surface chemistry of CO_2–Adsorption of carbon dioxide on clean surfaces at ultrahigh vacuum. *Progress in surface science*, 89(2):161–217, 2014.

[9] D. A. King and M. G. Wells. Molecular beam investigation of adsorption kinetics on bulk metal targets: Nitrogen on tungsten. *Surface Science*, 29(2):454 – 482, 1972.

[10] D. Kulginov, M. Persson, C. Åkerlund, I. Zorić, and B. Kasemo. CO_2 sticking on Pt(111): The role of kinetic energy and internal degrees of freedom. *Journal of Vacuum Science & Technology A*, 13(3):1511–1516, 1995.

[11] G.-C. Wang, L. Jiang, Y. Morikawa, J. Nakamura, Z.-S. Cai, Y.-M. Pan, and X.-Z. Zhao. Cluster and periodic DFT calculations of adsorption and activation of CO_2 on the Cu(hkl) surfaces. *Surface science*, 570(3):205–217, 2004.

[12] S.-G. Wang, D.-B. Cao, Y.-W. Li, J. Wang, and H. Jiao. Chemisorption of CO_2 on nickel surfaces. *The Journal of Physical Chemistry B*, 109(40):18956–18963, 2005.

[13] W. D. Mieher and W. Ho. Bimolecular surface photochemistry: Mechanisms of CO oxidation on Pt(111) at 85 K. *The Journal of Chemical Physics*, 99(11):9279–9295, 1993.

[14] C. Jansen and L. B. F. Juurlink. Absolute dissociation cross sections for D_2 dissociation on Pt steps. submitted.

[15] R. S. Smith and B. D. Kay. Desorption Kinetics of Carbon Dioxide from a Graphene-Covered Pt(111) Surface. *The Journal of Physical Chemistry A*, 123(15):3248–3254, 2019.

[16] H. Shakeel, H. Wei, and J. Pomeroy. Measurements of enthalpy of sublimation of Ne, N_2, O_2, Ar, CO_2, Kr, Xe, and H_2O using a double paddle oscillator. *The Journal of Chemical Thermodynamics*, 118:127 – 138, 2018.

[17] J. Derouin, R. G. Farber, and D. R. Killelea. Combined STM and TPD study of Rh(111) under conditions of high oxygen coverage. *The Journal of Physical Chemistry C*, 119(26):14748–14755, 2015.

[18] R. G. Farber, M. E. Turano, E. C. Oskorep, N. T. Wands, E. V. Iski, and D. R. Killelea. The Quest for Stability: Structural dependence of Rh(111) on oxygen coverage at elevated temperature. *The Journal of Physical Chemistry C*, 121(19):10470–10475, 2017.

[19] X. Feng, J. I. Cerdá, and M. Salmeron. Orientation-Dependent Interaction between CO_2 Molecules Adsorbed on Ru(0001). *The journal of physical chemistry letters*, 6(9):1780–1784, 2015.

[20] C. Dri, A. Peronio, E. Vesselli, C. Africh, M. Rizzi, A. Baldereschi, M. Peressi, and G. Comelli. Imaging and characterization of activated CO_2 species on Ni(110). *Physical Review B*, 82(16):165403, 2010.

[21] N. Moazzen-Ahmadi and A. McKellar. Spectroscopy of dimers, trimers and larger clusters of linear molecules. *International Reviews in Physical Chemistry*, 32(4):611–650, 2013.

[22] L. A. Miccio, M. Setvin, M. Müller, M. Abadía, I. Piquero, J. Lobo-Checa, F. Schiller, C. Rogero, M. Schmid, D. Sánchez-Portal, U. Diebold, and J. E. Ortega. Interplay between Steps and Oxygen Vacancies on Curved TiO2(110). *Nano Letters*, 16(3):2017–2022, 2016.

[23] E. Grånäs, B. Arndt, C. Seitz, M. Wagstaffe, and A. Stierle. Atomic scale step structure and orientation of a curved surface ZnO single crystal. *The Journal of Chemical Physics*, 152(7):074705, 2020.

[24] J. E. Ortega, G. Vasseur, I. Piquero-Zulaica, J. Raoult, M. A. Valbuena, S. Schirone, S. Matencio, A. Mugarza, and J. Lobo-Checa. Atomically precise step grids for the engineering of helical states. *arXiv preprint arXiv:1902.05777*, 2019.

[25] H. Davis and J. Noonan. Rippled relaxation in the (110) surface of the ordered metallic alloy NiAl. *Physical review letters*, 54(6):566, 1985.

[26] M. Kulawik, N. Nilius, H.-P. Rust, and H.-J. Freund. Atomic Structure of Antiphase Domain Boundaries of a Thin Al_2O_3 Film on NiAl (110). *Physical review letters*, 91(25):256101, 2003.

[27] C. Ellinger, V. Vonk, N. Khorshidi, A. Vlad, A. Stierle, and H. Dosch. In situ x-ray study of the oxidation of a vicinal NiAl(6,7,1) surface. *New Journal of Physics*, 11(11):113004, 2009.

[28] D. Mullins and S. Overbury. The structure and composition of the NiAl(110) and NiAl(100) surfaces. *Surface Science*, 199(1-2):141–153, 1988.